Brittle intergranular fracture of two-dimensional disordered solids as a random walk

L. Ponson,[1, *] Z. Shabir,[2] E. Van der Giessen,[3] and A. Simone[2]

[1]*Institut Jean Le Rond d'Alembert (UMR 7190),*
CNRS - Université Pierre et Marie Curie, 75005 Paris, France
[2]*Faculty of Civil Engineering and Geosciences, Delft University of Technology,*
P.O. Box 5048, 2600 GA Delft, The Netherlands
[3]*Zernike Institute for Advanced Materials, University of Groningen,*
Nyenborgh 4, 9747 AG Groningen, The Netherlands
(Dated: June 16, 2016)

We present results of a hybrid experimental and numerical investigation of the roughness of intergranular cracks in two-dimensional disordered solids. We characterize the statistical properties of a series of brittle cracks in situations where the characteristic scale of damage is much smaller than the grain size. We show that crack paths exhibit mono-affine scaling properties characterized by a roughness exponent $\zeta = 0.50 \pm 0.05$ that can be explained from linear elastic fracture mechanics in the limit of large samples. Our findings support the description of the roughening process in two-dimensional brittle disordered solids by a random walk and sheds light on the origin of the abnormally large exponents $\zeta = 0.6 - 0.7$ previously measured in 2D fractured specimens.

Deciphering the statistical properties of fracture surfaces has been a long-standing goal in condensed matter physics [1, 2]. This has been driven both by curiosity and by the exploration of microscopic failure mechanisms that govern the macroscopic resistance of materials. Fracture surfaces reflect the complex interaction of cracks with microscale material features, and therefore represent a ready-made pathway to explore these mechanisms. The observation of universal scaling behaviors on experimental fracture surfaces [3–5] has raised hope that a unified theoretical framework may capture fracture processes in disordered solids. However, such a theory is still missing and the physical origin of the remarkable scaling properties of cracks are still debated.

A major obstacle to overcome is the observation of abnormally large roughness exponents $\zeta > 0.5$ – or persistent fracture profiles – in both two-dimensional (2D) thin sheets and fully three-dimensional (3D) specimens, while linear elastic fracture mechanics (LEFM) predicts smaller exponents $\zeta \leq 0.5$ [1, 2]. This paradox could be understood in 3D solids thanks to the experimental evidence of fracture roughness with an anti-persistent behavior ($\zeta_{3D} \simeq 0.4$) or even logarithmic correlations ($\zeta_{3D} \simeq 0$) [6–9], in agreement with LEFM [10–12]. In these studies, and contrary to previous works on metallic alloy [4], mortar [13], wood [14] or quasi-brittle rock [15] where $\zeta_{3D} \approx 0.75$ were reported, fracture surfaces were investigated at scales *larger* than the characteristic size ℓ_{pz} of the damage processes taking place at the crack tip during crack growth, satisfying thus the assumption of *brittle* failure made in LEFM. This explanation was latter confirmed by the observation of two separate scaling regimes: (i) a damage-driven roughness at small scales
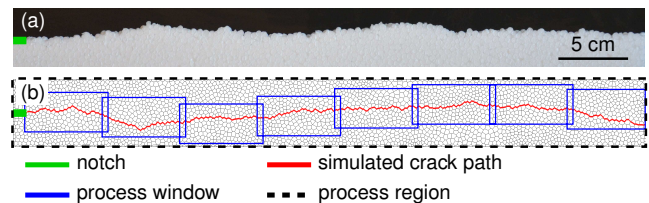
* laurent.ponson@upmc.fr

FIG. 1. (a) Brittle intergranular crack profiles obtained with experimental fracture tests of thin sheets of expanded polystyrene. (b) Large scale simulations of cohesive fracture of random arrangements of polygonal elastic grains.

with $\zeta_{3D} \approx 0.75$, and (ii) an LEFM-consistent roughness at larger scales, on the very same fracture surfaces of mortar [13], phase-separated glass [8], and subsequently on a large range of materials [16]. These results suggested fracture roughness, which has already been successfully applied to characterize material toughness from post-mortem fracture surface analysis [17], as an effective means to explore the characteristic length scales of damage in materials.

Surprisingly, such a level of understanding is far from being reached for the roughness of fractured 2D thin sheets. The pseudo-line tension of the crack front resulting from elasticity that dominates the roughening process in 3D brittle solids does not play any role in 2D [12, 18]. Instead, the crack trajectory in 2D solids is governed by the stress state near the tip which depends on the local crack inclination and the past trajectory [19]. These effects generally tend to maintain the crack path as close as possible to a straight line. Consequently, LEFM based models of crack propagation in disordered 2D solids predict anti-persistent fracture profiles, with $\zeta_{2D} \leq 0.5$, or even no self-affine regimes [20, 21]. These predictions are in contradiction with experiments that systematically re-

port exponents in the range $\zeta_{2D} \approx 0.6 - 0.7$ as in paper sheets [22–24], wood [25] or nickel-based alloy [26]. Recent numerical works that take into account the nucleation, growth and coalescence of damage cavities during the failure of 2D solids report values $\zeta = 0.65 - 0.70$ close to those obtained in experiments [27, 28]. This finding also compares with the predictions of random fuse and random beam models that describe qualitatively microcracking processes in quasi-brittle solids [29, 30]. If these results suggest that the persistent self-affine regime reported in experiments emerges from damage and microcracking processes, the existence of a scale invariant regime of roughness in *brittle* 2D thin sheets is still a matter of debate [20, 21]. The exploration of this regime on experimental and numerical examples is the central point of this Letter.

In the spirit of Refs. [7, 11], we consider 2D consolidated granular materials, characterized by intergranular failure, as archetypes of disordered brittle materials. Crack paths are investigated experimentally on nonporous thin sheets of polystyrene beads, and numerically in large scale 2D simulations of cohesive zone fracture of non-porous random arrangements of polygonal grains. The statistics of experimental and computed crack profiles is then fully characterized and shown to be reminiscent of the directed random walk with roughness exponent $\zeta = 1/2$. In the last part, we take inspiration from Ref. [20, 21], and propose a model of crack propagation through disordered brittle solids that is used to interpret our findings. Our study suggests a unified scenario for the morphology of fracture paths in 2D disordered solids that is discussed in the concluding section.

Experimental fracture tests of two-dimensional granular solids – In order to explore the crack morphology produced by brittle intergranular failure, we use commercial $30 \times 60 \text{ cm}^2$ panels of expanded polystyrene. Each panel consists of consolidated pre-expanded polystyrene beads with an average radius $\ell \simeq 2$ mm. The radius of the beads is comparable to the sample thickness, but is a few hundred times smaller than the other dimensions of the specimens. A 10 cm notch is machined at the center of one of the short edges of the plate and serves as the location of crack initiation. The experiments were conducted at constant displacement rate through a four-point bending device. This so-called *double torsion test* is classically used to achieve slow crack propagation under tensile (mode I) loading conditions in thin specimens [31]. In general, a groove is required to guide the crack parallel to the initial notch. However, straight crack propagation was achieved without it by applying four point forces, at equidistances 2.5 cm and 10 cm from the notch, on the top and bottom faces of the specimen. The bead cohesion was sufficiently low to ensure brittle intergranular failure as confirmed by *in situ* observations of the failure processes. Crack profiles were extracted using digital image analysis of pictures of the broken sample, an example of which is shown on Fig. 1(a).

Large scale simulations of intergranular failure based on sequential analyses – At variance with previous numerical studies on crack roughening in heterogeneous materials [32], here we investigate crack propagation in a material with a realistic microstructure by means of a numerical approach that reproduces fairly well the processes into play in experiments, namely intergranular brittle failure of random packings of grains.

Material parameters are taken to be representative of a polycrystalline alumina, Al_2O_3, which is described by means of Voronoi microstructures similar to that shown in Fig. 1(b). These microstructures are embedded in the process region of a notched specimen that is subsequently loaded by imposing uniform tensile stress on both sample faces parallel to the notch. This test geometry ensures crack propagation from the notch through the whole specimen with a straight trajectory on average. The boundary conditions of the test setup as well as the constitutive models for bulk and grain boundary behavior are identical to those reported in Ref. [33]. Although the numerical results have been obtained for a well defined polycrystalline material, they are expected to be representative of any consolidated granular material with zero porosity under the assumption that dissipative failure processes are confined to grain boundaries and embedded within a process zone of size ℓ_{pz} much smaller than the grain boundary length ℓ. Indeed, under these conditions, Shabir *et al.* [33] showed that the computed intergranular crack paths are not influenced by cohesive law parameters. This implies that in the limit of *brittle intergranular failure*, there exists a unique crack path for a given microstructure, irrespective of cohesive property values and material type.

Intergranular crack paths are computed with a Generalized Finite Element Method for polycrystals [34]. This method provides an accurate description of the stress field in a consolidated granular solid and yields reliable crack paths [33]. However, simulations of brittle failure with a number of grains which is large enough to explore the scaling properties of the corresponding crack profiles are prohibitively computationally expensive. To address this difficulty, a sequential analysis approach has been devised. The approach involves the division of a simulation into a suitable number of sub-simulations thus reducing the computational effort without sacrificing accuracy. In each sub-simulations, a process window (each of the regions enclosed by a blue line in Fig. 1(b)) is defined based on the extent of the non-linear region around the crack tip. This window follows the propagating crack tip and is relocated accordingly. A highly refined mesh, conforming to the procedure defined by Shabir *et al.* [33], is used around the crack tip in the process window. Outside it, a coarse mesh with at least two elements along each grain boundary is employed, and the grain boundaries are given a high stiffness to simulate perfect bond except those lying on the crack line which are given a zero elastic stiffness to simulate a traction-free crack. We have compared our approach with a monolithic approach on a series of granular topologies and the resulting
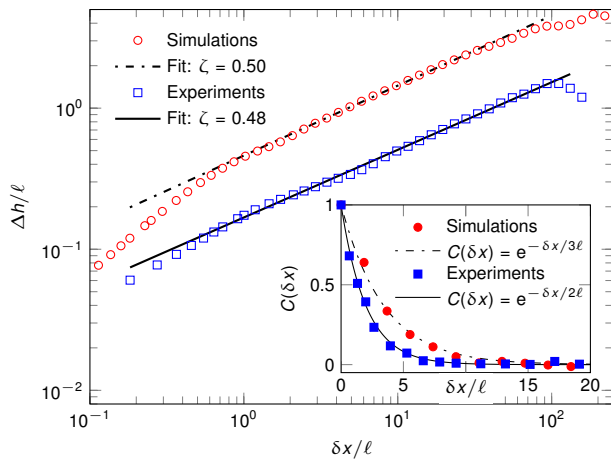
FIG. 2. Logarithmic representation of the height-height correlation function of the experimental and computed crack profiles. At scales larger than the microstructural scale ℓ, crack roughness is self-affine with an exponent $\zeta \simeq 0.50$. The inset shows the exponential decay of the correlation of the crack local slopes over a few length scales values ℓ, confirming the random walk behavior.
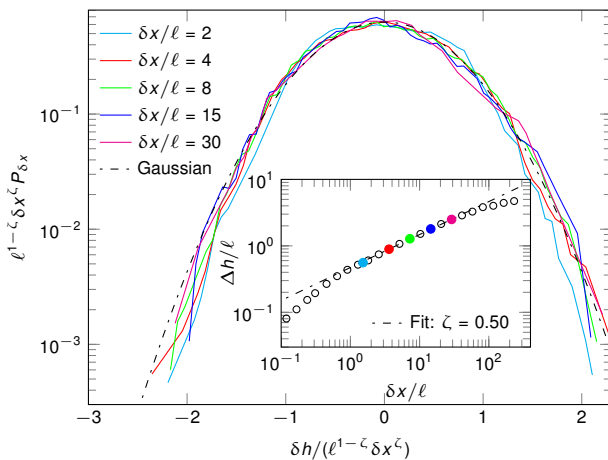

FIG. 3. Statistical distribution $P_{\delta x}$ of height variations computed for different scales δx. After normalization by δx^ζ with $\zeta = 0.50$, they collapse to a Gaussian distribution. The inset shows that the studied values of δx belong to the self-affine domain $\ell \lesssim \delta x \lesssim 100\,\ell$.

crack paths are identical. With this approach, detailed in Ref. [35], large crack propagation simulations can be carried out by considering a suitable number of cheaper sub-simulations. Fig. 1(b) shows a typical example with 3140 grains in the process region and about 320 broken grain boundaries.

Roughness characterization of the crack profiles – The statistics of the experimental and computed crack profiles are now investigated. We start by computing their height-height correlation function defined as $\Delta h(\delta x) = \langle [h(x + \delta x) - h(x)]^2 \rangle_x^{1/2}$, where δx is the increment to the spatial coordinate x. To take care of variations from

one sample to another, $\Delta h(\delta x)$ is averaged over six experimental and 18 simulated crack profiles. In the simulations, the grain arrangements consist of 3140 grains (Fig. 1(b)) and are obtained with a centroidal Voronoi tessellation algorithm. Fig. 2 shows the correlation functions of experimental and computed profiles. Both follow a power-law relation ($\Delta h(\delta x) \propto \delta x^\zeta$) which is reminiscent of self-affine properties characterized by the roughness exponent $\zeta_{\text{exp}} = 0.48 \pm 0.03$ for the experiments and $\zeta_{\text{sim}} = 0.50 \pm 0.02$ for the simulations. The errors are obtained from the roughness exponents computed on each profile analyzed separately. The self-affine behavior extends over a rather broad range of length scales, from the characteristic microstructural length ℓ to some upper bound $\delta x \approx 100\,\ell$. The value of the roughness exponent close to the directed random walk exponent $\zeta_{\text{rw}} = 1/2$ is confirmed by the behavior of the function $C(\delta x) = \langle h'(x + \delta x) h'(x) \rangle_x$ that shows no correlation of the crack local slopes on length scales $\delta x \gtrsim \ell$, as shown in the inset of Fig. 2.

The full roughness statistics of the simulated crack profiles, provided by the distributions $P_{\delta x}$ of the height fluctuations δh computed at some scale δx, are shown in Fig. 3. When normalized by δx^ζ with $\zeta = 0.50$, the distributions corresponding to different values of δx collapse to the same Gaussian distribution thus reflecting a mono-affine behavior which is obtained as long as δx belongs to the self-affine domain, as shown in the inset. Overall, our results indicate that the investigated cracks follow paths close to a directed random walk.

Theoretical interpretation – To understand this behavior, we derive a trajectory equation for a crack in an elastic medium with disordered fracture properties. Our model builds on basic concepts of LEFM, and in particular on the principle of local symmetry [19, 36] that predicts that cracks propagate along the direction of vanishing shearing mode II – note that even though specimens are loaded under pure mode I tension, the perturbations of the crack profile result in some local shearing in the crack tip vicinity. The crack path $h(x)$ is described as a succession of straight segments of size δx along the average propagation direction x. Following the idea of Katzav et al. [20, 21], we start from the calculation of Amestoy and Leblond [37] that predicts the kink angle between two successive incremental steps

$$\left.\frac{\mathrm{d}h}{\mathrm{d}x}\right|_{x^+} - \left.\frac{\mathrm{d}h}{\mathrm{d}x}\right|_{x^-} = -2\frac{k_{\text{II}}(x)}{k_{\text{I}}(x)}. \tag{1}$$

The local stress intensity factors $k_{\text{I}}(x)$ and $k_{\text{II}}(x)$ are calculated from the crack path configuration *before* the kink. We limit our analysis to slightly perturbed cracks $\mathrm{d}h/\mathrm{d}x \ll 1$ so we can use the results of Cotterel and Rice [19], completed by the ones of Movchan *et al.* [38], that provide $\{k_{\text{I}}^{\text{hom}}, k_{\text{II}}^{\text{hom}}\}$ as a function of the past trajectory $h(\tilde{x} < x)$, the macroscopic stress intensity factors $\{K_{\text{I}}, K_{\text{II}}\}$ imposed by the loading system to the specimen, and the coefficients $\{T, A\}$ of the higher order terms

in the development of the stress field near the tip:

$$\begin{cases} k_{\mathrm{I}}^{\mathrm{hom}}(x) = K_{\mathrm{I}} \\ k_{\mathrm{II}}^{\mathrm{hom}}(x) = K_{\mathrm{II}} + \dfrac{K_{\mathrm{I}}}{2}\left.\dfrac{\mathrm{d}h}{\mathrm{d}x}\right|_{x^-} - \sqrt{\dfrac{\pi}{2}}Ah(x) \\ \qquad\quad - \sqrt{\dfrac{2}{\pi}}\,T\displaystyle\int_{-\infty}^{x}\dfrac{\mathrm{d}h/\mathrm{d}x|_{\tilde{x}}}{\sqrt{x-\tilde{x}}}\,\mathrm{d}\tilde{x}. \end{cases} \quad (2)$$

Since in this study, the macroscopically applied shearing K_{II} is zero, combining Eqs. (1) and (2) yield to the following closed form of the path equation

$$\left.\frac{\mathrm{d}h}{\mathrm{d}x}\right|_{x^+} = \frac{2\sqrt{2}}{\sqrt{\pi}}\frac{T}{K_{\mathrm{I}}}\int_{-\infty}^{x}\frac{\mathrm{d}h/\mathrm{d}x|_{\tilde{x}}}{\sqrt{x-\tilde{x}}}\,\mathrm{d}\tilde{x} + \sqrt{2\pi}\frac{A}{K_{\mathrm{I}}}h(x). \quad (3)$$

For a homogeneous material, this equation admits a trivial stable solution, namely the straight crack path $h^{\mathrm{hom}}(x) = 0$, as both the T-stress and the value of A are negative in the specimen geometries considered here [19, 39]. To take into account spatial variations in the material fracture properties, one introduces the quenched noise $\delta k_{\mathrm{II}}^{\mathrm{het}} = -K_{\mathrm{I}}\,\eta(x)/2$ that describes the local shearing perturbations resulting from the material microstructure. As the materials considered display a random microstructure with a characteristic size ℓ, we consider *uncorrelated* quenched noise for length scales $\delta x \gg \ell$. Taking now into account both terms $k_{\mathrm{II}} = k_{\mathrm{II}}^{\mathrm{hom}} + k_{\mathrm{II}}^{\mathrm{het}}$ for predicting the kink angle from Eq. (1), one obtains

$$\left.\frac{\mathrm{d}h}{\mathrm{d}x}\right|_{x^+} = -\frac{1}{\sqrt{\mathcal{L}_1}}\int_{-\infty}^{x}\frac{\mathrm{d}h/\mathrm{d}x|_{\tilde{x}}}{\sqrt{x-\tilde{x}}}\mathrm{d}\tilde{x} - \frac{h(x)}{\mathcal{L}_2} + \eta(x) \quad (4)$$

where $\mathcal{L}_1$ and $\mathcal{L}_2$ are length scales emerging from the specimen geometry and the loading conditions that are calculated in the Supplemental Material [39]. Contrary to the model proposed in Refs. [20, 21], we do not consider variations of the elastic properties are rather homogenenous in the materials considered here. Instead, the out-of-plane excursions of the crack result from the variations of toughness, and more specifically from the randomly oriented weak planes embedded in the material granular microstructure. Note that a similar model was previously proposed, but in the context of cracks propagating through brittle materials with random fracture properties [10–12].

To characterize the geometry of the predicted crack profiles, the correlation of slopes is calculated from Eq. (4). As shown in the Supplementaly Material, the first and second term on the right hand side that are both inversely proportional to $\sqrt{\mathcal{L}_1} \gg \sqrt{\ell}$ and $\mathcal{L}_2 \gg \ell$, do not provide significant contributions, thus leading to

$$\langle \mathrm{d}h/\mathrm{d}x|_{x+\delta x} \times \mathrm{d}h/\mathrm{d}x|_x\rangle_x \simeq \langle\eta(x+\delta x)\times\eta(x)\rangle_x. \quad (5)$$

Local slopes of the crack profile have therefore the same correlator as η, and as such display no correlations at scales $\delta x \gg \ell$ larger than the grain size. This property characterizes a random walk: The predicted cracks are
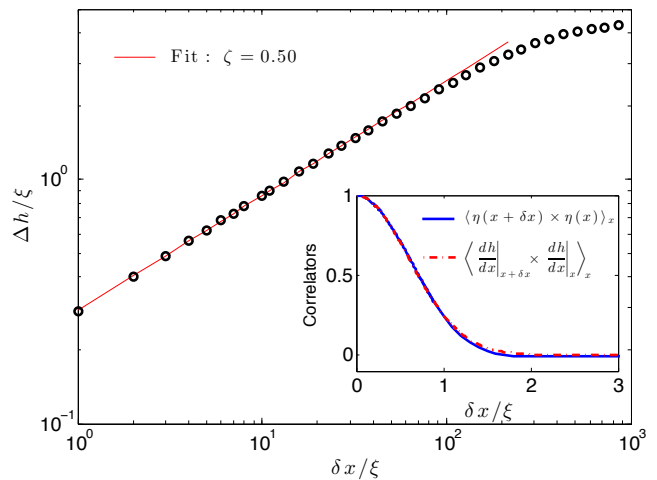

FIG. 4. Correlation function of the fracture profiles as predicted by the path equation (4) solved numerically. At large length scales $\delta x > \ell$, cracks follow a random walk with exponent $\zeta = 0.50$ (red straight line). In the inset, the correlator of the slopes of the predicted fracture profiles is compared with the correlator of η describing the material microstructure.

Gaussian self-affine profiles with a roughness exponent close to the random walk prediction $\zeta_{\mathrm{rw}} = 1/2$, in excellent agreement with the numerical and experimental observations. To describe more subbtle effects, like the saturation of the roughness Δh observed in Fig. 2 for $\delta x > 100\,\ell$, Eq. (4) is solved numerically using the values of $\mathcal{L}_1 \simeq 39\,000\,\ell$ and $\mathcal{L}_2 \simeq 500\,\ell$ corresponding to the loading conditions used in the simulations (see Supplemental Material). We use a short range disorder η with correlator $\langle\eta(x+\delta x)\times\eta(x)\rangle_x = \sigma^2\,e^{-\left(\frac{\delta x}{\ell}\right)^2}$ and amplitude $\sigma = 1$. As shown in Fig. 4, our model captures not only the scaling behavior of the crack path, but also the saturation of the roughness at large scales that reflects the finite size of the fracturing specimen. Finally, the inset of Fig. 4 shows the corresponding correlator of the local crack slopes that is, as expected from Eq. (5), close to the one chosen for the quenched noise.

Discussion – Our experimental and numerical observations, supported by the theoretical analysis based on LEFM proposed here, indicates that brittle cracks follow a directed random walks in 2D materials as long as the strutural length scales $\mathcal{L}_1$ and $\mathcal{L}_2$ are much larger than the characteristic microstructural length scale ℓ. More specifically, they are characterized by Gaussian fluctuations of height and a self-affine behavior of exponent $\zeta \simeq 0.50$ at scales larger than ℓ.

Then, how to concile our results with the observations of persistent fracture paths with $\zeta \simeq 0.6 - 0.7$ observed in paper [22–24], wood [25] or nickel-based alloy [26]? A key assumption of our model is the scale separation $\ell \gg \ell_{\mathrm{pz}}$ between the characteristic size ℓ of the microstructural disorder and the size ℓ_{pz} of the fracture process zone where damage mechanisms localize in

the crack tip vicinity. Indeed, LEFM assumes an elastic response everywhere in the material, and so $\ell_{\rm pz} = 0$. This assumption is satisfied in the fracturing materials investigated here, as the cohesive zone length chosen in the simulations and estimated in the experiments are much smaller than the grain size ℓ. On the contrary, the extent of the fracture process zone does compare with the characteristic microstructural feature in paper ($\ell \simeq 100\ \mu{\rm m} \lesssim \ell_{\rm pz} \simeq 1$ mm), wood ($\ell \simeq \ell_{\rm pz} \simeq 1-5$ mm) and nickel-based alloy ($\ell \simeq \ell_{\rm pz} \simeq 100\ \mu$m) for which a large exponent $\zeta \simeq 0.6-0.7$ was measured. These observations lead us to postulate the following scenario:

- For $\ell_{\rm pz} \ll \ell$, crack paths can be accurately described by LEFM and follow a directed random walk with exponent $\zeta = 0.50$ in the limit of large specimens, as shown in this letter.

- For $\ell_{\rm pz} \gg \ell$, the roughening process is dominated by the process of damage coalescence that takes place within the process zone. As shown by Bouchinder *et al.*[27], this crack growth mechanism is compatible with the persistent path with $\zeta \simeq 0.6-0.7$ observed experimentally in paper [22–24], wood [25] and alloy [26].

Interestingly, this scenario also accounts for the puzzling observation of random walk crack profiles with $\zeta \simeq 0.50$ in paper sheets perforated with holes [40], while fracture lines in virgin paper display $\zeta \simeq 0.65$. The upscaling of the characteristic size of the disorder, from the size of the fibers $\ell \simeq 100\ \mu$m to the interdistance $\ell \simeq 1\ \mu$mm between holes, may have shifted the roughening mechanism from a damage coalescence driven process to the brittle mechanism described in this study.

To conclude, we would like to highlight the remarkably simple features of brittle crack paths in large 2D specimens that show a Gaussian statistics of height fluctuations and a roughness exponent close to the random walk prediction $\zeta = {}^1\!/_2$. This behavior reminds the one of cracks in 3D brittle solids that also display Gaussian statistics and mono-affine properties with $\zeta \simeq 0.4 - 0.5$. This contrasts with fracture surface properties emerging from damage coalescence that display complex multi-affine features with fat-tail statistics both in 2D [41] and 3D materials [16, 42, 43]

[1] D. Bonamy and E. Bouchaud, Phys. Rep. **498**, 1 (2011).
[2] M. J. Alava, P. K. Nukala, and S. Zapperi, Adv. Phys. **55**, 349 (2006).
[3] B. B. Mandelbrot, D. E. Passoja, and A. J. Paullay, Nature **308**, 721 (1984).
[4] E. Bouchaud, G. Lapasset, and J. Planès, Europhys. Lett. **13**, 73 (1990).
[5] L. Ponson, D. Bonamy, and E. Bouchaud, Phys. Rev. Lett. **96**, 035506 (2006).
[6] J. M. Boffa, C. Allain, and J. P. Hulin, Eur. Phys. J. Appl. Phys. **2**, 281 (1998).
[7] L. Ponson, H. Auradou, P. Vié, and J. P. Hulin, Phys. Rev. Lett. **97**, 125501 (2006).
[8] D. Dalmas, A. Lelarge, and D. Vandembroucq, Phys. Rev. Lett. **101**, 255501 (2008).
[9] L. Ponson, H. Auradou, M. Pessel, V. Lazarus, and J.-P. Hulin, Phys. Rev. E **76**, 036108 (2007).
[10] S. Ramanathan, D. Ertas, and D. S. Fisher, Phys. Rev. Lett. **79**, 873 (1997).
[11] D. Bonamy, L. Ponson, S. Prades, E. Bouchaud, and C.Guillot, Phys. Rev. Lett. **97**, 135504 (2006).
[12] L. Ponson, Ann. Phys. **32**, 1 (2007).
[13] S. Morel, D. Bonamy, L. Ponson, and E. Bouchaud, Phys. Rev. E **78**, 016112 (2008).
[14] S. Morel, J. Schmittbuhl, J. M. Lopez, and G. Valentin, Phys. Rev. E **58**, 6999 (1998).
[15] S. Santucci, K. J. Måløy, A. Delaplace, J. Mathiesen, A. Hansen, J. Bakke, J. Schmittbuhl, L. Vanel, and P. Ray, Phys. Rev. E **75**, 016104 (2007).
[16] S. Vernède, L. Ponson, Y. Cao, and J.-P. Bouchaud, (submitted).
[17] A. Srivastava, L. Ponson, S. Osovski, E. Bouchaud, V. Tvergaard, and A. Needleman, J. Mech. Phys. Solids **63**, 62 (2014).
[18] H. Larralde and R. C. Ball, Europhys. Lett. **30**, 87 (1995).
[19] B. Cotterell and J. R. Rice, Int. J. Frac. **16**, 155 (1980).
[20] E. Katzav, M. Adda-Bedia, and B. Derrida, Europhys. Lett. **78**, 46006 (2007).
[21] E. Katzav and M. Adda-Bedia, Phys. Rev. E **88**, 052402 (2013).
[22] L. I. Salminen, M. Alava, and K. J. Niskanen, Eur. Phys. J. B **2003**, 369 (2003).
[23] J. Kertesz, V. Horvath, and F. Weber, Fractals **1**, 67 (1993).
[24] M. Mallick, P. P. Cortet, S. Santucci, S. G. Roux, and L.Vanel, Phys. Rev. Lett. **98**, 255502 (2007).
[25] T. Engøy, K. J. Måløy, A. Hansen, and S. Roux, Phys. Rev. Lett. **73**, 834 (1994).
[26] S. Morel, T. Lubet, J. L. Pouchou, and J. M. Olive, Phys. Rev. Lett. **93**, 065504 (2004).
[27] E. Bouchbinder, J. Mathiesen, and I. Procaccia, Phys. Rev. Lett. **92**, 245505 (2004).
[28] I. Ben-Dayan, E. Bouchbinder, and I. Procaccia, Phys. Rev. E **74**, 146102 (2006).
[29] S. Zapperi, P. K. V. V. Nukala, and S. Šimunović, Phys. Rev. E **71**, 026106 (2005).
[30] P. K. V. V. Nukala, S. Zapperi, M. J. Alava, and S. Šimunović, Phys. Rev. E **78**, 046105 (2008).
[31] B. K. Atkinson, J. Geophys. Res. **89**, 4077 (1984).

[32] M. J. Alava, P. K. N. N. Nukala, and S. Zapperi, Adv. Phys. **55**, 349 (2006).

[33] Z. Shabir, E. Van der Giessen, C. A. Duarte, and A. Simone, Modelling Simul. Mater. Sci. Eng. **19**, 035006 (2011).

[34] A. Simone, C. A. Duarte, and E. Van der Giessen, Int. J. Numer. Meth. Engng **67**, 1122 (2006).

[35] Z. Shabir, *Role of Microstructural Geometry in the Deformation and Failure of Polycrystalline Materials*, Ph.D. thesis, Delft University of Technology (2012), iSBN 978-94-6191-222-0.

[36] R. V. Gol'dstein and R. L. Salganik, Int. J. Frac. **10**, 507 (1974).

[37] M. Amestoy and J.-B. Leblond, Int. J. Solids Struc. **29**, 465 (1992).

[38] A. B. Movchan, H. Gao, and J. R. Willis, Int. J. Solids Struct. **35**, 3419 (1998).

[39] See Supplementary Material for the description of the experimental fracture tests, the calculation of the structural lengths $\mathcal{L}_1$ and $\mathcal{L}_2$, the perturbative resolution of the path equation and the detailed description of the simulations..

[40] O. Ramos, P.-P. Cortet, S. Ciliberto, and L. Vanel, Phys. Rev. Lett. **110**, 165506 (2013).

[41] E. Bouchbinder, I. Procaccia, S. Santucci, and L. Vanel, Phys. Rev. Lett. **96**, 055509 (2006) .

[42] L. Ponson, H. Auradou, M. Pessel, V. Lazarus, and J. P. Hulin, Phys. Rev. E **76**, 036108 (2007) .

[43] L. Ponson, Y. Cao, E. Bouchaud, V. Tvergaard, and A. Needleman, Int. J. Frac. **184**, 137 (2013) .

Brittle intergranular fracture of two-dimensional disordered solids as a random walk: Supplemental material

L. Ponson,[1, *] Z. Shabir,[2] E. Van der Giessen,[3, †] and A. Simone[2, ‡]

[1]*Institut Jean Le Rond d'Alembert (UMR 7190),*
CNRS - Université Pierre et Marie Curie, 75005 Paris, France
[2]*Faculty of Civil Engineering and Geosciences, Delft University of Technology,*
P.O. Box 5048, 2600 GA Delft, The Netherlands
[3]*Zernike Institute for Advanced Materials, University of Groningen,*
Nyenborgh 4, 9747 AG Groningen, The Netherlands
(Dated: June 16, 2016)

I. DESCRIPTION OF THE EXPERIMENTAL FRACTURE TESTS

The fracture experiments are performed using the so-called double torsion test, with dimensions $W \times L \times d = 30 \times 60 \times 1.5$ cm^3, which is shown schematically in Fig. 1. This geometry is classically used in experimental fracture mechanics to achieve slow and controlled mode I crack propagation under tensile loading conditions in thin specimens [1, 2]. In general, a groove is required to guide the crack parallel to the initial notch, which here has a length $c_0 = 10$ cm. However, straight crack propagation can be achieved without it by properly choosing the location of the application of the forces. Two point forces are applied from the top of the specimen on each side of the notch at a distance $w_2 = 2.5$ cm from it. Two parallel rails support the specimen from the lower side at a distance $w_1 = 10$ cm from the notch. To avoid indenting the specimen, the upper jaws are not directly in contact with the supper face of the sample, but apply a distributed force over an area of about 5 cm^2 thanks to a thin plate placed between the jaw and the specimen, as shown in Fig. 1(b). The upper jaw is displaced vertically at a constant velocity $v_{\text{ext}} = 0.1$ mm.s^{-1}, leading to a slow crack propagation until full failure of the specimen. During a test, the crack propagates over a total distance $\Delta c_{\text{tot}} \simeq 50$ cm that corresponds to about 250 polystyrene beads, allowing a rather extended domain of length scale to investigate the scaling properties of the crack path (see Fig. 2 in the main text).
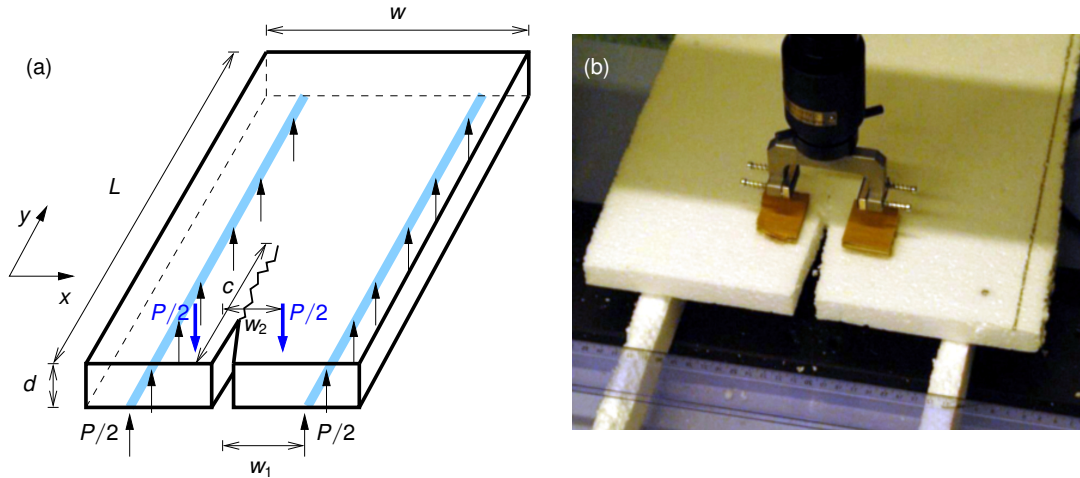

FIG. 1. Experimental setup: (a) Schematic representation of the fracture test. (b) Snapshot of the pre-notched specimen and the loading system. There is an error in the difinition of the axis: x must correspond to the propagation direction while y must be the normal direction to the crack.

---

* laurent.ponson@upmc.fr
† e.van.der.giessen@rug.nl
‡ a.simone@tudelf.nl

II.   EXPRESSION OF THE STRUCTURAL LENGTH SCALES $\mathcal{L}_1$ AND $\mathcal{L}_2$

The structural length scales involved in the path equation (4) of the main text emerges from the specimen geometry and the loading conditions. They are defined as

$$\begin{cases} \mathcal{L}_1 & = & \dfrac{\pi}{8} \left(\dfrac{K_{\mathrm{I}}}{T} \right)^2 \\[2mm] \mathcal{L}_2 & = & \dfrac{1}{\sqrt{2\pi}} \dfrac{K_{\mathrm{I}}}{A} \end{cases} \tag{1}$$

In these expressions, the stress intensity factor K_I, the T-stress and the quantity A correspond to the prefactors in the William's expansion of the stress field

$$\begin{cases} \sigma_{yy}(r) & = & \dfrac{K_{\mathrm{I}}}{\sqrt{2\pi r}} - A \sqrt{r} \\[2mm] \sigma_{xx}(r) & = & \dfrac{K_{\mathrm{I}}}{\sqrt{2\pi r}} - T \end{cases} \tag{2}$$

for a *straight* crack [3, 4] where r is the distance to the crack tip along the propagation direction x. σ_{yy} is the opening stress that drives the crack growth while σ_{xx} is the stress aligned with the propagation direction.

To obtain the values of K_{I}, T and A , and so $\mathcal{L}_1^{\mathrm{sim}}$ and $\mathcal{L}_2^{\mathrm{sim}}$ for the specimen geometry used in the *simulations*, we compute the stress field through finite element implementing the boundary conditions defined in Fig. 2. Note that both $\mathcal{L}_1$ and $\mathcal{L}_2$ are independant of the amplitude of the applied stress, so we consider a unit stress $\sigma = 1$ Pa in our simulations. The elements of the mesh are chosen so that their size decreases exponentially while approaching the crack tip, down to a minimum element size of $W/10^9$ where W is the specimen width. This allows capturing the square root divergence of the stress field whitout exceeding reasonable computational times, as the total node number can be maintained close to 5000. The variations of $\sigma_{\mathrm{yy}}(r)$ and $\sigma_{\mathrm{xx}}(r)$ are then fitted using the William's expension (2) following the procedure proposed in Ref. [5]: First, K_{I} is obtained from the square root divergence of the stress in the near tip region. Then, the leading term $K_{\mathrm{I}}/\sqrt{2\pi r}$ of the stress field expansion is substracted to the total stress so that the residuals $\Delta\sigma_{\mathrm{yy}}(r) = \sigma_{\mathrm{yy}}(r) - K_{\mathrm{I}}/\sqrt{2\pi r}$ and $\Delta\sigma_{\mathrm{xx}}(r) = \sigma_{\mathrm{xx}}(r) - K_{\mathrm{I}}/\sqrt{2\pi r}$ can be fitted by the affine functions $\Delta\sigma_{\mathrm{yy}} = -A R$ and $\Delta\sigma_{\mathrm{yy}} = -T - B R$ where $R = \sqrt{r}$. This provides the value of T and A, while B, that is not relevant for our analysis, is let aside. Finally, using the Eqs. (1), one obtains $\mathcal{L}_1^{\mathrm{sim}} = 40\,W$ and $\mathcal{L}_2^{\mathrm{sim}} \simeq W/2$ for a crack lying near the middle of the specimen of Fig. 2 as considered during the simulations. From the relation $W \simeq 1000\ell$ between the specimen width and the grain boundary length, one obtains structural lengths $\mathcal{L}_1^{\mathrm{sim}} = 40\,000\,\ell$ and $\mathcal{L}_2^{\mathrm{sim}} \simeq 500\,\ell$ that are much larger than the microstructural length.

To determine $\mathcal{L}_1^{\mathrm{exp}}$ and $\mathcal{L}_2^{\mathrm{exp}}$ in the case of the *experimental* fracture tests of Fig. 1, we follow a different procedure, as the bending conditions imposed to the specimen and the complex crack front geometry (see *e.g.* [6]) would have required a fully 3D finite element analysis of the stress field in the crack region. Instead, we estimate these length scales from analytical approximated formulas for K_{I}, T and A. In the double torsion test used in our experiments, the intensity factor at the tip of a straight crack follows $K_{\mathrm{I}} \simeq \dfrac{(w_1 - w_2)P}{d^2\sqrt{W}}$, [2]. An estimate of the T-stress can be obtained using the relation $T = \sigma_{\mathrm{xx}}^{(\mathrm{nc})} - \sigma_{\mathrm{yy}}^{(\mathrm{nc})}$ [4] where the superscript (nc) refers to the stress field calculated for the same geometry and loading conditions, but without crack. As the conditions are close to pure bending in the middle part of the specimen, the stress $\sigma_{\mathrm{xx}}^{(\mathrm{nc})}$ aligned with the crack propagation direction is close to zero while the stress $\sigma_{\mathrm{yy}}^{(\mathrm{nc})}$ can be estimated at the bottom surface of the specimen where the tensile state of stress drives the crack, leading to $T \simeq -\sigma_{\mathrm{yy}}^{(\mathrm{nc})} \simeq -\dfrac{(w_1 - w_2)P}{d^2 L}$, so that $\mathcal{L}_1^{\mathrm{exp}} \simeq \dfrac{L^2}{W}$ from Eq. (1). To estimate $\mathcal{L}_2^{\mathrm{exp}}$, we take inspiration from other fracture tests: In the thin strip geometry used in the simulations and analyzed in the previous paragraph, a finite element analysis of the stress field in the near tip region shows that $\mathcal{L}_2 \simeq W$. Similarly, in the double cleavage drilled compression test analyzed in Ref. [5], the third order term, proportional to $A \sim 1/\mathcal{L}_2$ in the Williams' expansion of the near tip field, is also set by the specimen width W. As a result, we assume a similar behavior for the bending test used in the experiments, so that $\mathcal{L}_2^{\mathrm{exp}} \simeq W$. This relation is supported by the physical intuition that the term $h/\mathcal{L}_2$ in the path equation (4) of the main text should be revelant when the crack "feels" the specimen boundary, *i..e.* for crack path excursions h of the same order as the specimen width.

The expressions of the structural lengths and their value expressed as a function of the microstructural scale ℓ,

namely the bead diameter in the experiments and the grain boundary length in the simulations, are

$$
\begin{cases}
\mathcal{L}_1^{\text{exp}} \simeq \dfrac{L^2}{W} \simeq 600\,\ell \quad \text{and} \quad \mathcal{L}_2^{\text{exp}} \simeq W \simeq 150\,\ell \\[3mm]
\mathcal{L}_1^{\text{sim}} \simeq \dfrac{L^2}{W} \simeq 40\,500\,\ell \;\; \text{and} \quad \mathcal{L}_2^{\text{sim}} \simeq W \simeq 500\,\ell.
\end{cases}
\tag{3}
$$

III. PERTURBATIVE RESOLUTION OF THE PATH EQUATION

We now introduce the variables

$$
\epsilon_1 = \sqrt{\ell/\mathcal{L}_1} \quad \text{and} \quad \epsilon_2 = \ell/\mathcal{L}_2
\tag{4}
$$

that are equal to $\epsilon_1^{\text{sim}} \simeq 0.005$ and $\epsilon_2^{\text{sim}} \simeq 0.002$ in the simulation and $\epsilon_1^{\text{exp}} \simeq 0.04$ and $\epsilon_2^{\text{exp}} \simeq 0.007$ for the experiments. Using the change of variables

$$
\begin{cases}
w &= x/\ell \\
f(x) &= h(x/\ell)/\ell \\
\gamma(x) &= \eta(x/\ell),
\end{cases}
\tag{5}
$$

we can rewrite the path equation (4) of the main text as

$$
\left.\frac{\mathrm{d}f}{\mathrm{d}w}\right|_{w^+} = -\epsilon_1 \int_{-\infty}^{w} \frac{f'(\tilde{w})}{\sqrt{w-\tilde{w}}}\,\mathrm{d}\tilde{w} - \epsilon_2\, f(w) + \gamma(w).
\tag{6}
$$

where f and w are dimensionless and provide the crack perturbation and the distance along the mean crack path in units of ℓ, respectively. The small values of ϵ_1 and ϵ_2 indicate that they can be used as small parameters to perturbatively solve the path equation in the context of the fracture tests performed in this work. Thus we seek a solution in the form

$$
f(w) = f^{(0)}(w) + \epsilon_1 f_1(w) + \epsilon_2 f_2(w).
\tag{7}
$$

Inserting this expression into the path equation (6) and separating zeroth order terms from those proportional to ϵ_1 or ϵ_2 we find[1][2]

$$
\begin{cases}
\left.\dfrac{df^{(0)}}{dw}\right|_{w^+} &= \gamma(w) \\[3mm]
\epsilon_1 \dfrac{df_1}{dw} + \epsilon_2 \dfrac{df_2}{dw} &= -\epsilon_1 \mathcal{I}(w) - \epsilon_2 \dfrac{f^{(0)}(w)}{\ell}
\end{cases}
\tag{8}
$$

where $\mathcal{I}(w) = \displaystyle\int_{-\infty}^{w} \frac{f'^{(0)}(\tilde{w})}{\sqrt{w-\tilde{w}}}\,d\tilde{w}$. Coming back to the original variables, the zeroth order equation gives

$$
\left.\frac{dh^{(0)}}{dx}\right|_{x^+} = \eta(x).
\tag{9}
$$

We remind that the term η describes the local shear perturbations resulting from the material microstructure. We therefore expect it to behave as a short range correlated quenched noise. As a result, the solution $h^{(0)}$ of the zeroth order equation predicts a directed random walk. This is consistent with the numerical and experimental observations reported in this study.

––––––––

[1] EvdG to LP: Why distinguish between dh/dx and h' ? I have corrected this and use now only the notation dh/dx

[2] EvdG to LP: Since only $\mathcal{L}_1$ depends on L what is L?, I do not think that ϵ_1 and ϵ_2 can be considered as independent variables. Thus I would conclude $dh_1/dh = -\mathcal{I}(x)$ and $dh_2/dh = h^{(0)}(x)/\ell$. Do you disagree? I don't consider ϵ_1 and ϵ_2 as independant variables: I just assume that they are both small with respect to one.
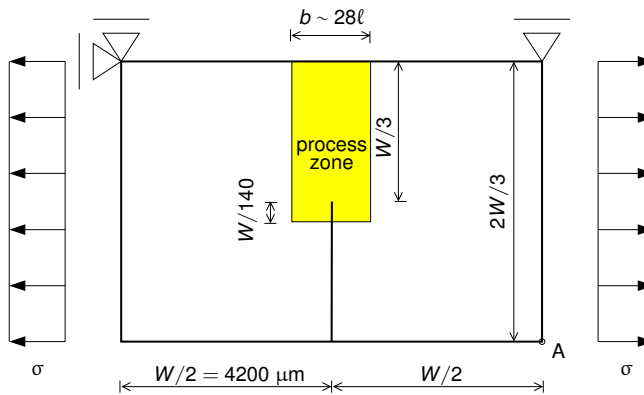
FIG. 2. Geometry and boundary conditions for the notched specimen employed in the simulations.

We now seek to determine the correlation function of the local slopes along the crack path which, using the decomposition (7), but for the original quantities $h(x) = h^{(0)}(x) + \epsilon_1 h_1(x) + \epsilon_2 h_2(x)$, reads

$$
\begin{aligned}
C(\delta x) &= \langle h'(x) h'(x + \delta x)\rangle_x \\
&= \langle h'^{(0)}(x) h'^{(0)}(x + \delta x)\rangle_x \\
&+ \langle h'^{(0)}(x) [\epsilon_1 h_1'(x + \delta x) + \epsilon_2 h_2'(x + \delta x)]\rangle_x \\
&+ \langle h'^{(0)}(x + \delta x) [\epsilon_1 h_1'(x) + \epsilon_2 h_2'(x)]\rangle_x + ...
\end{aligned}
\tag{10}
$$

Using $\epsilon_1 \ll 1$ and $\epsilon_2 \ll 1$, the terms proportional to ϵ_1 and ϵ_2 can be neglected, so that only the first line that writes as $C(\delta x) = C_\eta(\delta x) = \langle \eta(x)\eta(x + \delta x)\rangle_x$ after using Eq. (9). The correlator of the local slopes therefore coincides with the one of the quenched disorder, so it is is essentially zero for $\delta x > \ell$, as also observed in our experiments and simulations.[3]
[4]

IV. LARGE SCALE SIMULATIONS OF INTERGRANULAR FAILURE THROUGH SEQUENTIAL ANALYSES AND THE GENERALIZED FINITE ELEMENT METHOD

V. TEST SETUP AND MATERIAL

The geometry and boundary conditions of the test setup are reported in Fig. 2. The material parameters are taken to be representative of an average polycrystalline alumina, Al_2O_3, with Young's modulus $E = 384.6$ GPa and Poisson's ratio $\nu = 0.237$. Plane strain analyses are performed under the assumption of small elastic strains and rotations. The notched specimen is loaded by a uniform tensile stress, σ, which is ramped incrementally under quasi-static loading conditions. A centroidal Voronoi tessellation algorithm is used to generate 18 different topologies of 3140 grains each. Voronoi arrangements are embedded in the process zone shown in Fig. 2. An average grain size of approximately 20 μm has been used. This size corresponds to an average grain boundary length ℓ of 10.62 μm. The number of grain boundaries in front of the notch tip is around 320 on average and this implies that the number of cracked grain boundaries will be around the same figure.

The linear elastic isotropic grains are connected to each other by means of cohesive grain boundaries which follow the Xu-Needleman cohesive law [7] incorporating secant unloading and reloading behavior. According to Shabir et al. [8], intergranular crack paths in brittle polycrystals are unique for a given microstructure, irrespective of cohesive law parameters. Following this argument, the mode-I fracture energy, G_{Ic}, and the maximum normal cohesive strength, σ_{max}, are set equal to 39.6 Jm^{-2} and 0.6 GPa, respectively. With this set of cohesive law parameters, relatively coarse meshes can resolve the cohesive law along grain boundaries.

---

[3] EvdG: meaning of tilde in $\tilde{x}$? This is the variable of integration
  EvdG: Upon more careful reading it looks like $\tilde{x}$ is just an auxiliary coordinate parallel to x. But so is u. Would it make sense to use u here instead of $\tilde{x}$? Just to iron out unnecessary variables .... It is now corrected

[4] EvdG to LP: It is not entirely clear to me if we need this paragraph. The main text only states Eq. (6), i.e. eq. (11) from the SM neglecting terms proportional to ϵ_1 and ϵ_2. The relevance of these latter terms is briefly discussed in the subsequent paragraph, which I'm afraid I don't quite understand (Angelo's comment in footnote ?? makes sense to me too). What about including the part until Eq. (9) and then simply say that the terms proportional to ϵ_1 and ϵ_2 are negligible since they are small, see SM Eq. (2)? I agree

A. Generalized Finite Element Method for polycrystals

Crack paths are computed using a Generalized Finite Element Method for polycrystals [9]. In this approach, a polycrystal is obtained by the superposition of a polycrystalline topology on a simple background finite element mesh which, unlike in the classical finite element method, does not need to conform to the local features of the topology. This superposition is automatically handled using the partition of unity property of finite element shape functions hence automating the mesh generation stage. Being an advanced version of the standard Finite Element Method (FEM), this method provides an accurate description of the stress field around a propagating crack tip in polycrystalline materials and therefore predicts reliable crack paths [8].

B. Sequential polycrystalline analysis

The determination of the roughness exponent calls for computational approaches that can deliver accurate crack paths in polycrystalline aggregates with a large number of grains. Accuracy of the crack path is ensured by requiring a sufficiently refined mesh along grain boundaries and around triple junctions [8]. These meshing requirements result in simulations that cannot be handled using traditional fully resolved monolithic analyses. Without recurring to sophisticated approaches [?], we have developed a simple sequential polycrystalline analysis approach to trace the crack path in polycrystalline aggregates with a large number of grains. The method involves the division of a simulation into a suitable number of sub-simulations. The approach is illustrated in Fig. 3 by means of a 90-grain topology which has been analyzed in three different ways using the specimen in Fig. 2. For reference, the first simulation uses a highly refined mesh along each grain boundary (GB) following the rules suggested by Shabir et al. [8]. This is depicted in Fig. 3(a) where final and traction-free (notch line in this case) crack lines[5] are shown in red and green colors, respectively. The load-displacement curve is presented in Fig. 3(e). Based on this analysis, a von Mises equivalent stress plot after a short crack extension is reported in Fig. 3(b). In this plot, an active process zone can be defined based on the extent of the non-linear region around the crack tip. This window follows the propagating crack tip and is relocated accordingly.[6] In the second analysis, we allowed non-linearities from the cohesive law within the active process zone only. Outside this window, the grain boundaries are given a high stiffness to simulate perfect bond except those lying on the crack line which are given a zero elastic stiffness to simulate a traction-free crack. This analysis yielded the same crack path and load displacement curve as obtained in the first analysis (cf Figs. 3(a) and (e)). From this result, it can be deduced that a highly refined mesh is needed only in the active process zone to account for the non-linearities. The region outside the active process zone, following mostly a linear elastic behavior, can be discretized with a coarser mesh. Following this argument in our third analysis, we split the simulation into a sequence of sub-simulations. In this academic example we consider two sub-simulations as follows:

1. A highly refined mesh as proposed in [8] is provided around the crack tip in the active process zone. Outside this region, at least two elements are provided along each grain boundary. Both regions can be seen in Figs. 3(c) and (d) for each sub-simulation.

2. When a crack tip reaches the end of an active process zone in the crack propagation direction, the simulation is stopped and the resulting crack profile is saved —the crack path obtained from simulation 1 is indicated by the red line in Fig. 3(c). The next sub-simulation is launched considering the saved crack profile from the previous simulation —the green line in Fig. 3(d). A new crack tip is defined by reducing the length of the loaded crack profile such that the new tip is now at a position where the cohesive strength of the previous simulation would be negligible —the green line in Fig. 3(d) has a reduced length than the length of the corresponding red line in Fig. 3(c). In other words, we make sure that nonlinear processes are accurately captured by enclosing nonlinear regions with an active process zone. We have found that an overlap of $\sim 2.5\ell$ between two consecutive active process zones satisfies this requirement with the current choice of cohesive law and parameters.

The sequential polycrystalline analysis yielded the same crack path as reported in Fig. 3(a) which was obtained with the first monolithic analysis. The equivalence of this analysis to the monolithic analysis can also be appreciated from the load-displacement curves shown in Fig. 3(e). In this figure, the curves related to the two sub-simulations follow the curve from the first analysis in their respective domains. With regards to the stress field, we could hardly find any difference between the two analyses.

---

[5] ERIK TO ANGELO: I'm afraid this (especially to gather with the legend in Fig. 3a) may be confusing as it sounds like the simulated crack is not traction free. What about initial notch (or crack) in green and simulated crack in red?

[6] ERIK TO ANGELO: I think there is a jump in the logic here. In my understanding the idea is to use this moving process zone in the second (new) simulation.
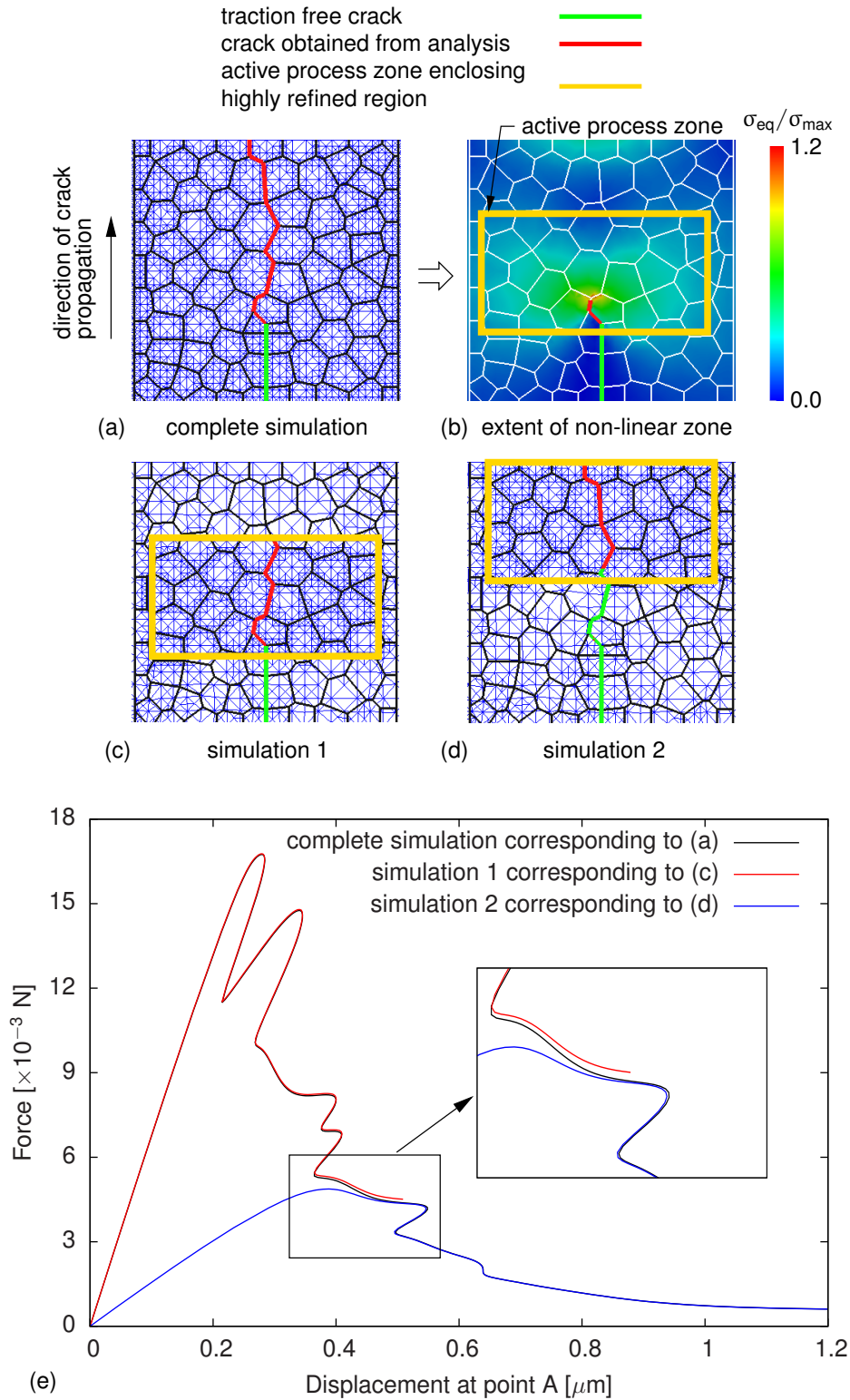
FIG. 3. Sequential polycrystalline analysis of a 90-grain topology: (a) highly refined mesh with final crack path; (b) von Mises equivalent stress corresponding to the simulation in (a) with an active process zone defined approximately considering the extent of non-linear region around a typical crack tip as shown; (c and d) sub-simulation 1 and 2 with a highly refined mesh in the active process zone —at least two elements along each grain boundary are provided outside the active process zone; (e) load-displacement curves corresponding to the simulations in (a), (c) and (d). Only the process zone is showed in (a) to (d).
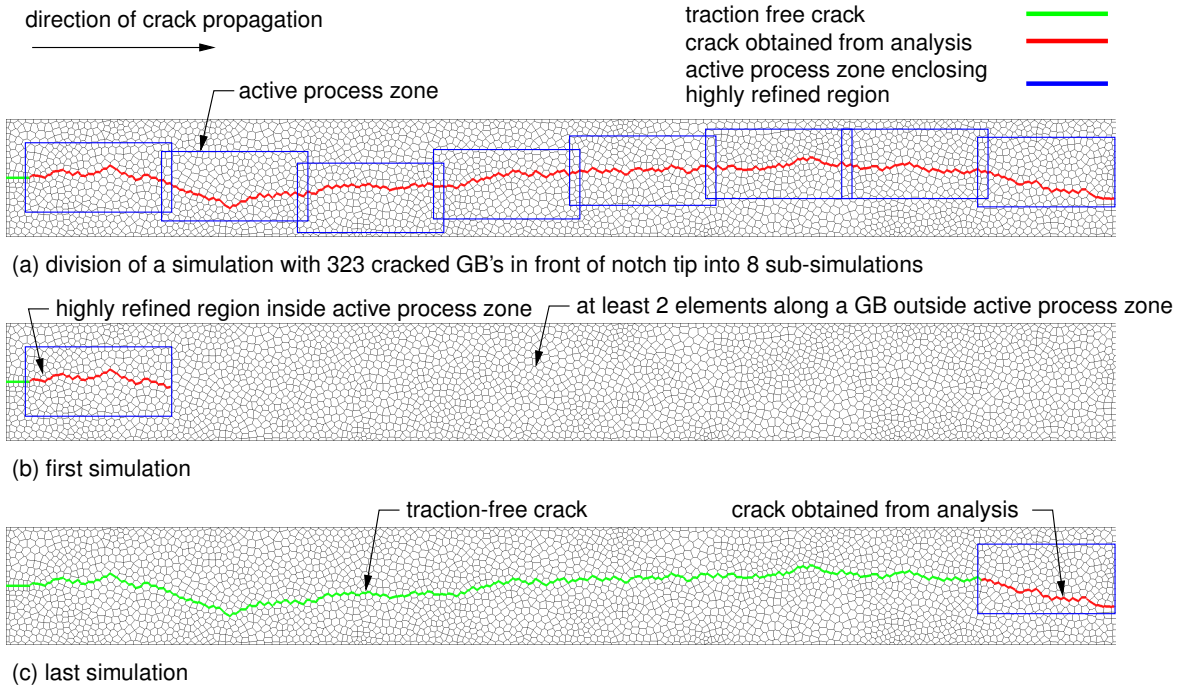
(a) division of a simulation with 323 cracked GB's in front of notch tip into 8 sub-simulations

(b) first simulation

(c) last simulation

FIG. 4. Sequential polycrystalline analysis of a 3140-grain topology. Only the process zone is showed. For convenience, the process zone has been rotated by $-90°$.
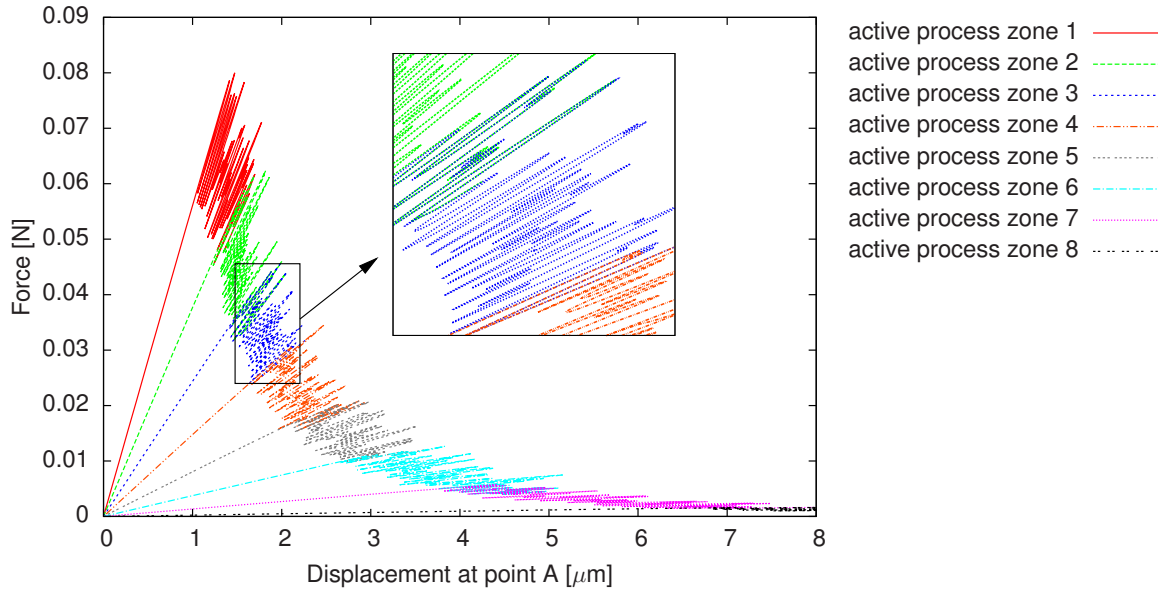

FIG. 5. Load-displacement curves obtained through sequential polycrystalline analysis for the 3140-grain topology depicted in Fig. 4.

With this approach, large crack propagation simulations can be carried out by considering a suitable number of computationally-doable sub-simulations. A typical example employing a 3140-grain topology and eight sub-simulations is shown in Fig. 4(a) with the first and last sub-simulation reported in Figs. 4(b) and (c), respectively. The blue boxes in these figures are the active process zone which show the area where the crack is allowed to propagate within a sub-simulation. The corresponding load-displacement curves for all the eight sub-simulations are reported in Fig. 5. From the inset in this figure, the complexity of the analysis, overwhelmed by many sharp snap-backs, can be easily

recognized —it is worth noticing that each jump in the curve corresponds to the fracture of one grain boundary.

Unlike classical adaptive refinement approaches [10–12], the only information that is transferred from simulation to simulation is the crack path. We have compared our approach with a monolithic approach on a series of polycrystalline topologies and the resulting crack paths are identical.

———————————————————————

[1] B. K. Atkinson, J. Geophys. Res. **89**, 4077 (1984).
[2] A. G. Evans, J. Mater. Sci. **15**, 1137 (1972).
[3] B. Cotterell and J. R. Rice, Int. J. Frac. **16**, 155 (1980).
[4] A. B. Movchan, H. Gao, and J. R. Willis, Int. J. Solids Struct. **35**, 3419 (1998).
[5] G. Pallares, L. Ponson, A. Grimaldi, M. Georges, G. Prevot, and M. Ciccotti, Int. J. Frac. **156**, 11 (2009).
[6] M. Ciccotti, J. Am. Ceram. Soc. **83**, 2737 (2000).
[7] X.-P. Xu and A. Needleman, J. Mech. Phys. Solids **42**, 1397 (1994).
[8] Z. Shabir, E. Van der Giessen, C. A. Duarte, and A. Simone, Modelling Simul. Mater. Sci. Eng. **19**, 035006 (2011).
[9] A. Simone, C. A. Duarte, and E. Van der Giessen, Int. J. Numer. Meth. Engng **67**, 1122 (2006).
[10] M. Ortiz and J. J. Quigley IV, Comput. Methods Appl. Mech. Engrg. **90**, 781 (1991).
[11] F.-J. Barthold, M. Schmidt, and E. Stein, Comp. Mech. **22**, 225 (1998).
[12] H. Cramer, M. Rudolph, G. Steinl, and W. Wunderlich, Compt. Struct. **73**, 61 (1999).